Antiferromagnetism of CeCd$_{0.67}$As$_2$ existing deep inside the narrow gap semiconducting state

Suyoung Kim [1], Obinna P. Uzoh [1], and Eundeok Mun [1,2]

[1]*Department of Physics, Simon Fraser University, Burnaby, Canada, BC V5A 1S6*

[2]*Center for Quantum Materials and Superconductivity (CQMS), Sungkyunkwan University, Suwon 16419, South Korea*

Single crystals of RCd$_{0.67}$As$_2$ (R = La and Ce) have been synthesized by a high-temperature ternary melt and their physical properties have been explored by means of magnetization, specific heat, electrical resistivity, Hall coefficient, and thermoelectric power measurements. RCd$_{0.67}$As$_2$ compounds indicate a (structural) phase transition at high temperatures, accompanied by a remarkable increase of the electrical resistivity with an extremely low carrier concentration. CeCd$_{0.67}$As$_2$ exhibits a large magnetic anisotropy and an antiferromagnetic (AFM) order below $T_N = 4$ K. Magnetic susceptibility curves, together with magnetization isotherms and specific heat, are analyzed by the point charge model of the crystalline electric field (CEF). In the paramagnetic state, the observed magnetic properties can be well explained by the CEF effects, implying that the $4f$ moments remain localized. Electrical resistivity measurements, together with Hall resistivity and thermoelectric power, also suggest highly localized $4f$ electrons, where Kondo contributions are negligible. The low-temperature physical properties manifest strong magnetic field dependencies. For $H \perp c$, T_N shifts to lower temperature as magnetic field increases and eventually disappears at $H_c \sim 60$ kOe. Inside the AFM state, three metamagnetic transitions are clearly evidenced from the magnetization isotherms. The RKKY interaction may be responsible for the AFM ordering in CeCd$_{0.67}$As$_2$; however, it would have to be mediated by extremely low charge carriers. Although the AFM ordering temperature in CeCd$_{0.67}$As$_2$ can be continuously suppressed to zero, no AFM quantum phase transition is expected due to the lack of conduction electron clouds to screen the $4f$ moments.

I. INTRODUCTION

Ce-based intermetallic compounds have shown a variety of interesting phenomena, such as heavy fermion (HF) behavior [1], valence fluctuation [2], unconventional superconductivity [3–6], and quantum phase transitions [7–9]. These interesting phenomena are related to the hybridization between localized $4f$ electrons and conduction electrons. A strong hybridization delocalizes the $4f$ electron, pushing the system into a paramagnetic Kondo state, whereas a weaker hybridization results in an antiferromagnetic (or ferromagnetic) order via Ruderman-Kittel-Kasuya-Yosida (RKKY) interaction. When the Doniach-like diagram is considered, a general assumption is that the system contains a sufficiently large amount of conduction electrons to screen the local moments and to mediate a coupling between the localized $4f$ moments. An interesting question is how does the low carrier density affect these phenomena [10,11]. Because the low carrier density means a lack of conduction electrons to either screen the moments or mediate the interaction between moments, both RKKY and Kondo interactions are expected to be weakened. There are only a small fraction of low-carrier-density $4f$ HF systems, such as CeNiSn, CeRhSn, Ce$_3$Pt$_3$Bi$_4$, CeNi$_{2-x}$As$_2$, and Yb$_3$Ir$_4$Ge$_{13}$ [12–17]. Strongly correlated electronic states in low-carrier Kondo lattice systems, more recently exploring also unconventional quantum criticality, continue to attract considerable attention [15–20]. To enhance our knowledge in such a regime, studies of more materials are needed.

We have systematically studied the physical properties of RCd$_{0.67}$As$_2$ (R = La and Ce) systems to investigate RKKY and Kondo interactions deep inside the low-carrier, semiconducting state. RCd$_{0.67}$As$_2$ compounds belong to a large number of ternary pnictides RTX_2 (R = rare earth, T = transition metal, X = As, Sb, and Bi) [21–26]. Many of these compounds typically adopt the tetragonal HfCuSi$_2$-type structure ($P4/nmm$, Z = 2, no. 129). Among these series the ternary antimonides with T = Ag showed that all atomic positions are fully occupied [21], while a deficiency of the transition-metal site frequently occurs, corresponding to the formula $RT_{1-x}X_2$, due to the distortion of X square nets [25,27–29]. In addition, an excess of the transition-metal site can also be observed, as seen in RCu$_{1+x}$As$_2$ [30]. In the ternary arsenides RTAs$_2$, crystal structure and physical properties have been previously investigated for T = Cu [21], Cd [31], and Zn [25]. The RCuAs$_2$ compounds form a tetragonal HfCuAs$_2$ structure and show an anomalous transport property [32,33]. It has been reported that LaZn$_{0.67}$As$_2$ crystallizes into a body-centered tetragonal SrZnBi$_2$-type structure ($I4/mmm$, Z = 4, no. 139), while RZn$_{1-x}$As$_2$ (R = Ce − Sm) forms a defect HfCuSi$_2$-type structure [25]. In particular, the structural refinement of PrZn$_{0.67}$As$_2$ found an ordering of a vacant Zn site, forming an ordered superstructure of Pr$_3$Zn$_2$As$_6$ ($Pmmn$, Z = 2, no. 59) [28]. Interestingly, the

electrical resistivity of $LaZn_{0.67}As_2$ shows an activated behavior (semiconductorlike behavior) arising from an energy gap [25].

In this manuscript we report the crystal structure, thermodynamic, and transport properties of $RCd_{0.67}As_2$ (R = La and Ce). Single crystals of these compounds have been synthesized by a high-temperature ternary melt with excess of Cd and As. At high temperatures, physical property measurements confirm a (structural) phase transition ($T_s = 280$ K for R = La and $T_s = 137$ K for R = Ce), and transport property measurements point to a semiconducting state below T_s with a low carrier density. The observed high-temperature magnetic property of $CeCd_{0.67}As_2$ can be well understood in the framework of the crystalline electric field (CEF) effect. We demonstrate that the CEF ground state of Ce $4f$ electron is an antiferromagnetic doublet with $T_N = 4$ K. It is of interest to explore antiferromagnetism existing deep inside the narrow gap semiconducting phase to see whether they are similar to or different from those found in good metallic systems. Recently, the existence of nonstoichiometric $RCd_{0.67}As_2$ (R = La and Ce) and their physical properties have been reported [31,34], where the compounds are synthesized in single-crystalline form by chemical vapor transport (CVT) technique. Both La- and Ce-based compounds crystallize into a vacancy-ordered superstructure of the body-centered tetragonal ($I4/mmm$) parent structure, corresponding to $R_3Cd_2As_6$ stoichiometry. As temperature is decreased, both compounds display the phase transition at $T = 136$ K and 278 K for $Ce_3Cd_2As_6$ and $La_3Cd_2As_6$, respectively, where these phase transitions are attributed to the charge density wave (CDW)–driven structural distortions. $Ce_3Cd_2As_6$ exhibits an antiferromagnetic ordering below $T_N = 4$ K, which increases to 5.3 K under external pressure of 3.8 GPa [34].

II. EXPERIMENTS

Single crystals of $RCd_{0.67}As_2$ (R = La and Ce) were grown out of a ternary melt with excess As and Cd. The constituent elements of high-purity La (Ce), Cd, and As, taken in the ratio $R_{0.04}(Cd_{0.44}As_{0.56})_{0.96}$, were placed in an alumina crucible and sealed in a silica ampoule under a partial Ar pressure. Initially, the ampoule was heated slowly to 450 °C in a box furnace, the temperature maintained for 5 h, and then was finally heated to 950 °C over 24 h. After being held for 1 h at 950 °C, the ampoule was slowly cooled down to 800 °C over 100 h. After removing the excess liquid by centrifuging, shiny single crystals were obtained (see insets of Fig. 1). Note that when the initial Cd composition is higher than the As composition and the temperature is raised above 1000 °C, hexagonal RCd_3As_3 phases are stabilized [35]. The crystal structure of the samples was confirmed by powder x-ray diffraction (XRD) at room temperature. Figure 1 shows XRD patterns of powdered $LaCd_{0.67}As_2$ and single-crystal $CeCd_{0.67}As_2$. No major differences in x-ray patterns are observed between R = La and Ce, except a shift of peak positions due to differences in the unit-cell volume.

The peak positions in powder XRD patterns can be well indexed with a monoclinic structure ($C2/m$, no. 12), which is reported to be a vacancy-ordered superstructure of the tetragonal $SrZnBi_2$-type structure ($I4/mmm$, no. 139) [25,31].
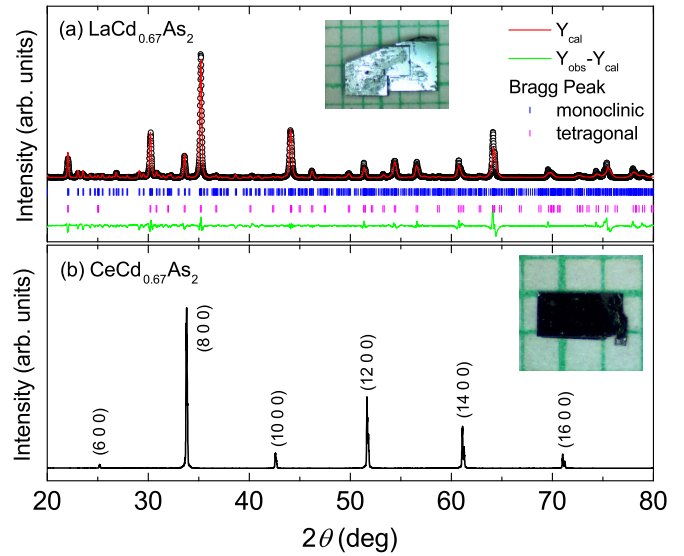

FIG. 1. (a) Powder XRD patterns of $LaCd_{0.67}As_2$. The red line is the calculated XRD patterns with a monoclinic structure ($C2/m$). Green lines represent the difference between the data and calculated XRD patterns. The Bragg positions are shown for both monoclinic (top) and tetragonal (bottom) structure. Inset shows a photograph of as-grown $LaCd_{0.67}As_2$ single crystal on a mm grid. (b) Single-crystal x-ray patterns for $CeCd_{0.67}As_2$. The peak indices (h, 0, 0) are in the monoclinic structure. Inset shows a photo of $CeCd_{0.67}As_2$ over the mm scale.

The obtained unit-cell parameters in monoclinic structure are $a = 21.7408$ Å, $b = 4.0995$ Å, $c = 12.3220$ Å, $\alpha = \gamma = 90°$, and $\beta = 100.96°$ for $LaCd_{0.67}As_2$; and $a = 21.6126$ Å, $b = 4.0528$ Å, $c = 12.2154$ Å, $\alpha = \gamma = 90°$, and $\beta = 100.71°$ for $CeCd_{0.67}As_2$. When the high-intensity peaks (main peaks) are only considered, the Bragg reflections of both La- and Ce-based compounds can be indexed in a tetragonal $SrZnBi_2$-type structure [25,31]. Unit-cell parameters refined for the tetragonal $SrZnBi_2$-type representation are obtained to be $a = b = 4.1052$ Å and $c = 21.3444$ Å for R = La, and $a = b = 4.0689$ Å and $c = 21.2363$ Å for R = Ce, values which are consistent with a previous report [31]. The grown single crystals form plates, as shown in the insets of Fig. 1, where well-formed edge facets are clearly visible. The observation of only (h, 0, 0) peaks, as shown in Fig. 1(b), confirms that the crystallographic a axis in the monoclinic structure is perpendicular to the plane of the plates. The (h, 0, 0) reflections in the monoclinic representation correspond to the (0, 0, l) reflections in the tetragonal representation. For the physical property measurements we use the tetragonal representation to denote the magnetic field orientations: $H \parallel c$ and $H \perp c$. Note that the magnetic field orientation $H \perp c$ is either $H \parallel [100]$ or [010], otherwise specified.

The dc magnetization was measured in a Quantum Design (QD) Magnetic Property Measurement System (MPMS) up to 70 kOe. The specific heat, C_p, was measured by the relaxation technique down to $T = 1.8$ K in a QD Physical Property Measurement System (PPMS). Four-probe dc resistivity measurements were performed in a QD PPMS with the current flowing perpendicular to the c axis. Due to the high contact

resistance, of the order of $\sim$30 Ω at room temperature, a current of less than 1 μA was applied below the phase transition (T_s) to avoid sample heating. Hall resistivity measurements were performed in a four-wire geometry, where the current was flowing normal to the c axis and the magnetic field was applied to the c axis. To remove magnetoresistance effects due to voltage-contact misalignment, the magnetic field directions were reversed. It has to be noted that due to the very large longitudinal resistivity contribution caused by the voltage contact misalignment, the Hall resistivity was measured only down to 50 K. Thermoelectric power measurements were performed with two thermometer and one heater configuration in a homemade setup.

III. RESULTS AND DISCUSSION

The magnetic susceptibility of LaCd$_{0.67}$As$_2$ reveals remarkable temperature dependences, with a hint of a (structural) phase transition and a hysteresis. Figure 2(a) shows anisotropic magnetic susceptibility curves, $\chi(T) = M/H$, below 350 K at $H=70$ kOe, applied both perpendicular ($H\perp c$) and parallel ($H \parallel c$) to the c axis in the tetragonal representation of the crystal structure. M/H of LaCd$_{0.67}$As$_2$ depends weakly on temperature with a small magnitude, where the absolute value of magnetic susceptibility for $H \perp c$ is roughly twice bigger than that for $H \parallel c$. M/H curves for both orientations indicate a jump with a small hysteresis loop between 280 and 290 K as a signature of a (structural) phase transition (inset). Note that the jumps seen in M/H for two different orientations are in opposite direction, implying anisotropic change of either Landau diamagnetism or Pauli paramagnetism. M/H for $H \parallel c$ clearly indicates a hysteresis between 70 and 150 K while warming and cooling, whereas the hysteresis for $H \perp c$ is negligible.

At low temperatures, M/H curves for both field orientations show an upturn, most likely due to the presence of paramagnetic impurities, consistent with the magnetic field dependence of magnetization at 2 K as shown in Fig. 2(b). Magnetization isotherms, $M(H)$, at $T = 300$ K decrease quasilinearly with increasing magnetic field up to 70 kOe for both orientations, whereas $M(H)$ curves at $T = 2$ K show a hump at around 10 kOe, probably due to the presence of paramagnetic impurities, and indicate basically linear field dependences above 20 kOe. It should be noted that the slope in the linear field regime at 2 K is the same as that at 300 K. $M(H)$ curves at 2 K show no hysteresis, while increasing and decreasing magnetic field for both $H \perp c$ and $H \parallel c$ directions.

A jump observed in M/H through 280 $\sim$ 290 K is clearly confirmed as a phase transition from the specific heat measurements. The temperature dependence of the specific heat, $C_p(T)$, curves of LaCd$_{0.67}$As$_2$ are shown in Fig. 3, where C_p data are taken for both warming and cooling. A well-defined λ-shaped anomaly at $\sim$280 K on top of a broad background between 280 and 290 K is clearly seen (inset), confirming the phase transition. This high-temperature anomaly shows no magnetic field dependence up to $H = 90$ kOe applied for $H \parallel c$, as shown in the bottom inset. The phase transition temperature, corresponding to the sharp peak position at $T_s = 280$ K, is consistent with an earlier report [31]. However, the

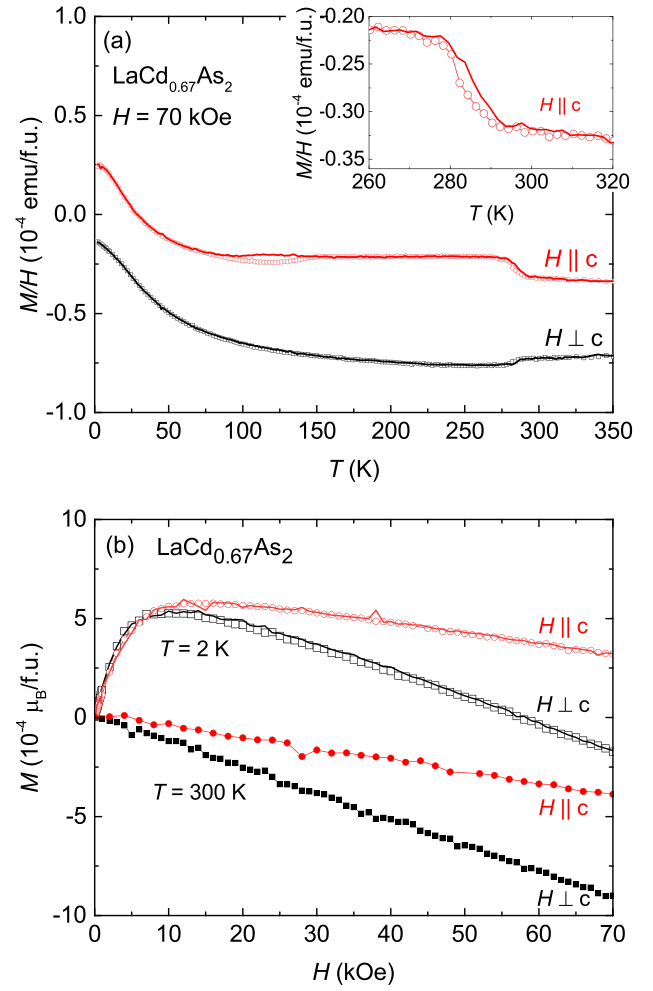FIG. 2. (a) M/H of LaCd$_{0.67}$As$_2$ for both $H \parallel c$ and $H \perp c$. The magnetic field orientations are based on the tetragonal representation. Symbols and lines indicate the up-sweep and down-sweep of temperature, respectively. Inset shows an enlarged plot between 260 and 320 K for $H \parallel c$. (b) $M(H)$ at 2 and 300 K. Symbols and lines indicate the up-sweep and down-sweep of the magnetic field, respectively.

broad maximum underneath the peak observed in this study (flux-grown sample) was not identified in an earlier study on a La$_3$Cd$_2$As$_6$ sample grown by the CVT technique [31]. Although the origin of the broad background is currently unclear, we conjecture that this is related to the distortion of As-square net [36] and the sample inhomogeneity.

Above T_s, the absolute value of C_p reaches $\sim$90 J/mol K, which is somewhat lower than the Dulong-Petit limit. Unlike the magnetic susceptibility for $H \parallel c$, C_p indicates no hysteresis between 70 and 150 K. Since the specific heat curve follows $C_p(T) = \gamma T + \beta T^3$ in a limited temperature range (top inset), the electronic and phonon contributions are estimated by fitting the curve below 2.5 K. The electronic contribution and Debye temperature are estimated to be $\gamma \sim 0.036$ mJ/mol K^2 and $\Theta_D \sim 283$ K, respectively, consistent with an earlier study [31]. The small γ value suggests either a very small effective mass or low carrier density in this material.
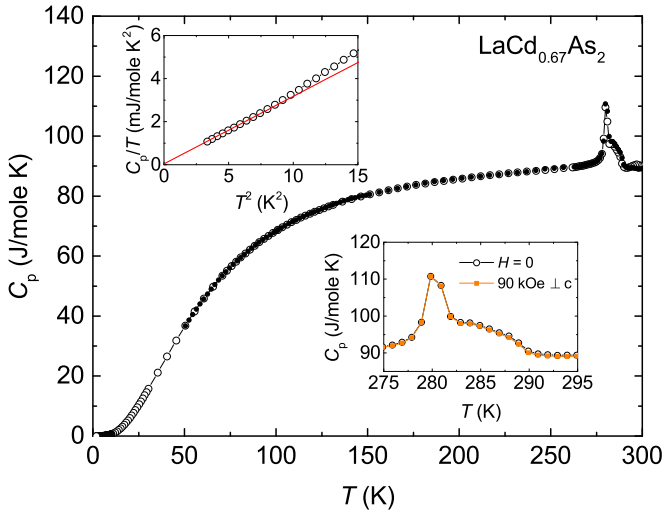
FIG. 3. C_p of LaCd$_{0.67}$As$_2$ in zero field. Top inset shows C_p/T vs T^2 plot. The solid line represents the linear fit below 2.5 K. Bottom inset shows an enlarged plot near the phase transition at $H = 0$ and 90 kOe for $H \perp c$.

The temperature dependence of the electrical resistivity curves, $\rho(T)$, of LaCd$_{0.67}$As$_2$ are shown in Fig. 4(a) at $H = 0$ and 90 kOe for $H \perp c$, where the resistivity measurements are performed while warming and cooling. In zero field, $\rho(T)$ indicates three distinctive behaviors: a jump below 290 K with minor hysteresis, a pronounced hysteresis between 70 and 152 K, and a semiconductorlike increase below 70 K. $\rho(T)$ at 90 kOe shows a negative magnetoresistance below 70 K, while no magnetic field dependence is shown above 70 K. It has to be noted that $\rho(T)$ of CVT-grown La$_3$Cd$_2$As$_6$ indicates a remarkable increase of 13 orders of magnitude below the phase transition at 279 K [31], which is in sharp contrast to the flux-grown sample.

A large resistivity value and rapid increase of resistivity below 70 K suggest a low carrier concentration in LaCd$_{0.67}$As$_2$. To estimate the carrier concentration, the Hall resistivity, ρ_H, is measured as a function of temperature at 90 kOe for $H \parallel c$. The temperature dependence of the Hall coefficient, $R_H = \rho_H/H$, is plotted in Fig. 4(b). The open symbol and solid line indicates R_H measurements while warming and cooling the temperature, respectively. As the temperature decreases, the R_H curve shows a very weak slope change at $\sim$280 K, reveals a hysteresis loop between 90 and 152 K, and drastically decreases below the hysteresis, which is consistent with $\rho(T)$ behavior. The sharp change in R_H can be related to the decreasing carrier density. Based on the one-band model approximation, the carrier density is estimated to be $\sim$1.29$\times$10^{21} per cm^3 at 300 K and $\sim$5.5$\times$10^{18} per cm^3 at 50 K, which corresponds to $\sim$0.12 carrier per formula unit (f.u.) at 300 K and $\sim$0.0005 carrier per f.u. at 50 K, confirming the low-carrier-density material. Thus the negligibly small γ value can be related to the low carrier density in LaCd$_{0.67}$As$_2$. The negative sign of R_H indicates that transport is dominated by electronlike carriers, which is consistent with thermoelectric power (TEP) measurement.
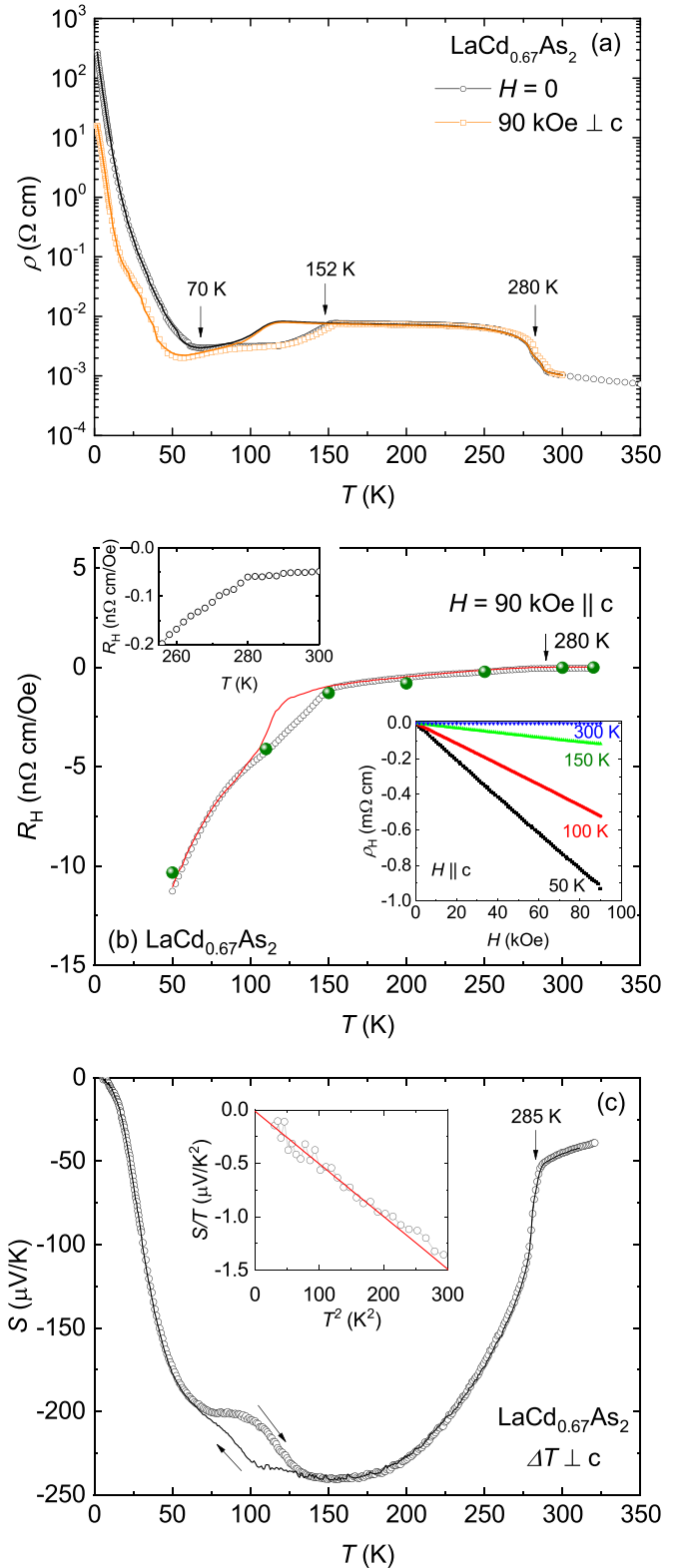

FIG. 4. (a) $\rho(T)$ of LaCd$_{0.67}$As$_2$ at $H = 0$ and 90 kOe for $H \perp c$. (b) R_H at 90 kOe for $H \parallel c$. Open symbol and line indicates R_H taken while warming and cooling, respectively. Solid symbols are taken from the magnetic field sweep while cooling the sample. Top inset shows R_H near 280 K. Bottom inset shows Hall resistivity ρ_H at selected temperatures. (c) Zero field $S(T)$, taken while warming and cooling. Inset shows S/T vs T^2 plot.

As a further probe of the transport property, TEP, LaCd$_{0.67}$As$_2$ has been measured as a function of temperature, $S(T)$, plotted in Fig. 4(c). $S(T)$ indicates a sharp drop below 285 K and shows a parabolic temperature dependence with a pronounced hysteresis loop between 70 and 132 K. The minimum in $S(T)$ occurs near 150 K with $-240\ \mu$V/K. The observed TEP value of LaCd$_{0.67}$As$_2$ is an order of magnitude higher than the one in typical metals and close to the typical values of narrow gap semiconductors [37–39]. Below 150 K the rapid variation in $S(T)$ can be related to the thermal depopulation of charge carriers. In a multiband system, the Seebeck coefficient is given by the Seebeck coefficient of each band weighted by the electrical conductivity of each band [40]. Therefore, to explain the strong temperature dependence of TEP, both the carrier density and mobility of each band must be properly accounted for.

At low temperatures, $S(T)$ can be very well described by the $aT + bT^3$ relation, as shown in the inset, where the first and second term represent the electronic and phonon contribution, respectively. By fitting the curve below 10 K (inset), the electronic contribution is estimated to be $a = -1.28 \times 10^{-8}$ V/K^2. The small value of a yields the Lorentz ration $q = aN_Ae/\gamma \sim -34$, where the constant $N_Ae = 9.6 \times 10^4$ C/mol is the Faraday number [40]. The obtained large q value implies a low carrier density of the LaCd$_{0.67}$As$_2$ system, which is consistent with Hall effect measurements. In general, $S(T)$ of typical metals shows a maximum corresponding to the phonon-drag effect, where the maximum is expected to be located between $\Theta_D/5$ and $\Theta_D/12$ [41]. $S(T)$ of LaCd$_{0.67}$As$_2$ indicates an absence of the low-temperature broad peak caused by the phonon drag.

Thermodynamic and transport property measurements of LaCd$_{0.67}$As$_2$ clearly indicate the phase transition below 280 K. It has been shown that the distortion of As- and Sb-square net in this family of materials induces a metal-to-semiconductor transition [25,36,42]. Since LaCd$_{0.67}$As$_2$ compound has no moment bearing ions, the anomaly cannot be related to magnetic origin but can be associated with electronic structure change and/or structural phase transition. In a CVT-grown La$_3$Cd$_2$As$_6$ sample, a sharp phase transition at 279 K has been attributed to a CDW transition caused by a distortion in the arsenic square net [31]. Among these family of materials, CDW transition has been identified from exceptionally clean LaAgSb$_2$ single crystal [43]. We tentatively anticipate that the discrepancy between CVT and flux-grown samples could be associated with structural features like different levels of local atomic distortions and Cd site vacancies. In addition, we conjecture that additional features observed below T_s in transport properties of LaCd$_{0.67}$As$_2$ are related to further structural distortions and a superstructure that may change the electronic properties over the temperature range measured. In the superstructure of RTAs$_2$ (T = Zn and Cd), the vacancy ordering at the zinc site of the primitive tetragonal HfCuSi$_2$-type structure forms an orthorhombic ($Pmmn$) superstructure (Pr$_3$Zn$_2$As$_6$) [28], whereas the Cd vacancy ordering of the body-centered tetragonal ZrZnBi$_2$-type structure forms a monoclinic ($C2/m$) superstructure (R_3Cd$_2$As$_6$) [31]. Therefore it is necessary to perform high-energy x-ray experiments to understand the observed physical properties of the flux-grown LaCd$_{0.67}$As$_2$ sample.

Inverse magnetic susceptibility, $1/\chi(T) = H/M$, curves of CeCd$_{0.67}$As$_2$ are shown in Fig. 5(a), applied magnetic fields for both $H \perp c$ and $H \parallel c$, and a polycrystalline average in the tetragonal representation. The polycrystalline average is estimated as $\chi_{poly} = 2/3\ \chi_{\perp c} + 1/3\ \chi_c$. It should be emphasized that although the signature is not pronounced, magnetic susceptibility curves, especially for $H \parallel c$, clearly indicate a jump at $T_s \sim 137$ K as a signature of the phase transition (see inset). H/M for $H \perp c$ follows a linear temperature dependence above 200 K, whereas H/M for $H \parallel c$ shows no clear, linear temperature dependence up to 375 K, probably due to the CEF effects. To estimate the effective moment μ_{eff} and Weiss temperature θ_p, we fit the curve by the Curie-Weiss law, $\chi(T) = C/(T - \theta_p)$, from the linear region of the H/M curves: $\mu_{eff}^{\perp c} = 2.55\ \mu_B$ and $\theta_p^{\perp c} = 5.3$ K for $H \perp c$; $\mu_{eff}^c = 2.92\ \mu_B$ and $\theta_p^c = -442.7$ K for $H \parallel c$; and $\mu_{eff}^{poly} = 2.58\ \mu_B$ and $\theta_p^{poly} = -34.7$ K for χ_{poly}. Note that for $H \parallel c$ the fit was performed within the limited temperature range from 350 to 375 K. It is necessary to measure magnetic susceptibility above 375 K to determine μ_{eff}^c and θ_p^c more reliably along the c axis. The magnetic susceptibility results in this study are consistent with the earlier report [34].

At low temperatures, $\chi(T)$ clearly indicates an AFM ordering below 4 K. The low-temperature $\chi(T)$ data, measured for $H \perp c$, are plotted in Fig. 5(b) for various applied magnetic fields. The AFM ordering temperature T_N, determined from the $d\chi T/dT$ analysis, is consistent with the earlier study [34]. With increasing magnetic field, T_N shifts to lower temperatures and suppresses below 1.8 K for $H > 60$ kOe. In the derivatives, two slope changes appear above 10 kOe and only one peak shows above 35 kOe. Above 60 kOe, $\chi(T)$ does not reveal any signature of phase transitions and instead shows a tendency toward saturation at low temperatures. Note that for $H \parallel c$, T_N is hardly affected by the applied magnetic field.

The $M(H)$ measurements, shown in Fig. 5(c), shed further light on the low-temperature magnetic states of CeCd$_{0.67}$As$_2$. The $M(H)$ curves at 1.8 K are highly anisotropic between $H \perp c$ ($H \perp [001]$) and $H \parallel c$ ($H \parallel [001]$). It is clear from the figure that in-plane anisotropy is small. $M(H)$ for $H \parallel [001]$ increases almost linearly up to $\sim$0.13 μ_B/Ce^{3+} at 70 kOe. On the other hand, $M(H)$ for $H \parallel [100]$ linearly increases up to 19 kOe and then undergoes three metamagnetic (MM) transitions and appears to be approaching saturation at 70 kOe with a moment of $\sim$1.25 μ_B/Ce^{3+}. The MM transitions at $H = 19$, 34, and 58 kOe are clearly indicated in the dM/dH analysis as shown in the inset. $M(H)$ for both $H \parallel [100]$ and [010] clearly indicates three MM transitions, whereas only two MM transitions are observed for $H \parallel [110]$. It has to be noted that in the earlier study [34] two MM transitions at 19 and 34 kOe were only identified in the $M(H)$ curve for $H \perp c$ at 2 K. The magnetization value at 70 kOe is consistent with the earlier report [34] but lower than the theoretical value of 2.14 μ_B/Ce^{3+} for the saturated moment of free Ce^{3+} ions. Interestingly, no hysteresis is observed through the MM transitions.

The specific heat of CeCd$_{0.67}$As$_2$, plotted in Fig. 6(a), manifests λ-shape anomalies at 137 and 4 K, confirming phase transitions observed in M/H. Because of the AFM order below 4 K, γ and Θ_D of CeCd$_{0.67}$As$_2$ cannot be reliably obtained by using the relation $\gamma T + \beta T^3$. Instead, $\gamma = 13$ mJ/mol K^2
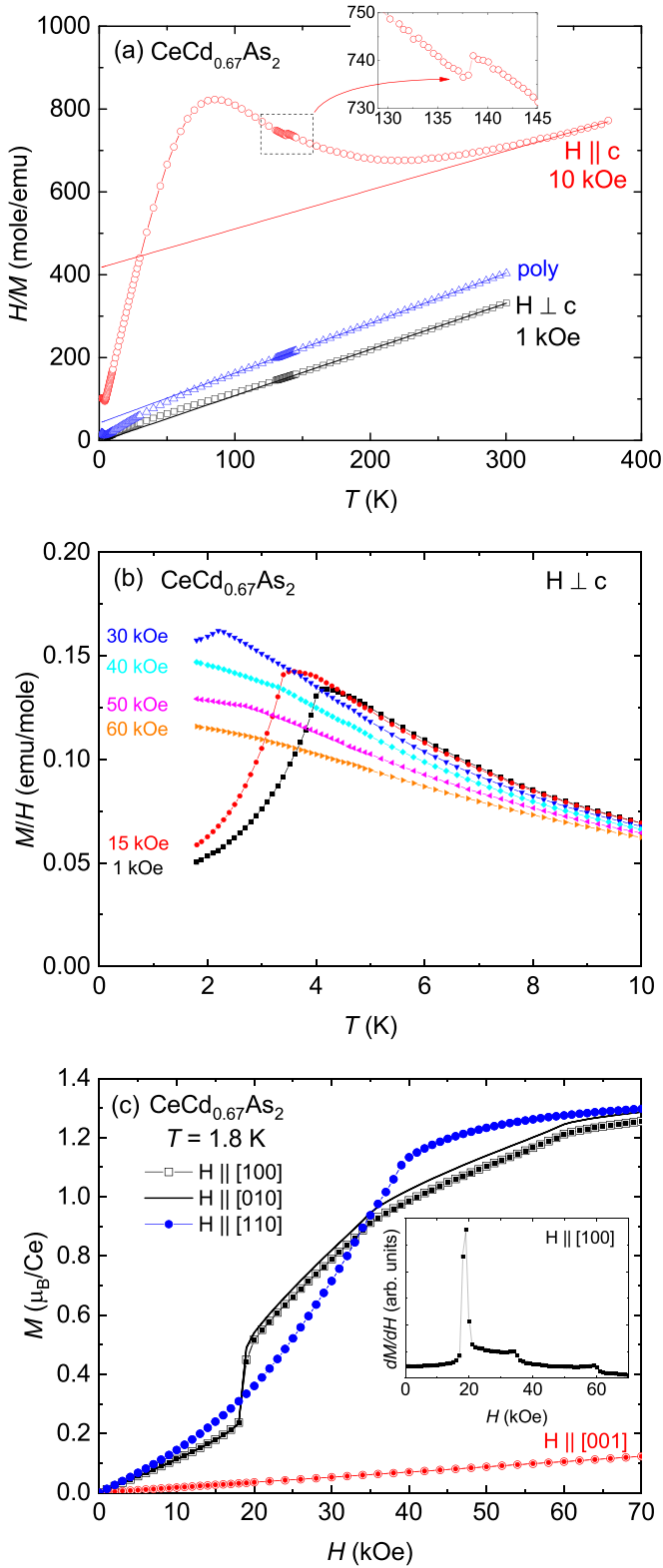
FIG. 5. (a) Inverse magnetic susceptibility H/M of CeCd$_{0.67}$As$_2$ for $H \perp c$, $H \parallel c$, and poly average crystalline. Solid lines represent C-W fit. (b) M/H of CeCd$_{0.67}$As$_2$ for $H \perp c$ at selected magnetic fields. (c) Magnetization isotherms at 1.8 K for $H \parallel$ [100], [010], [110], and $H \parallel$ [001] in the tetragonal representation. Inset shows dM/dH for $H \parallel$ [100].
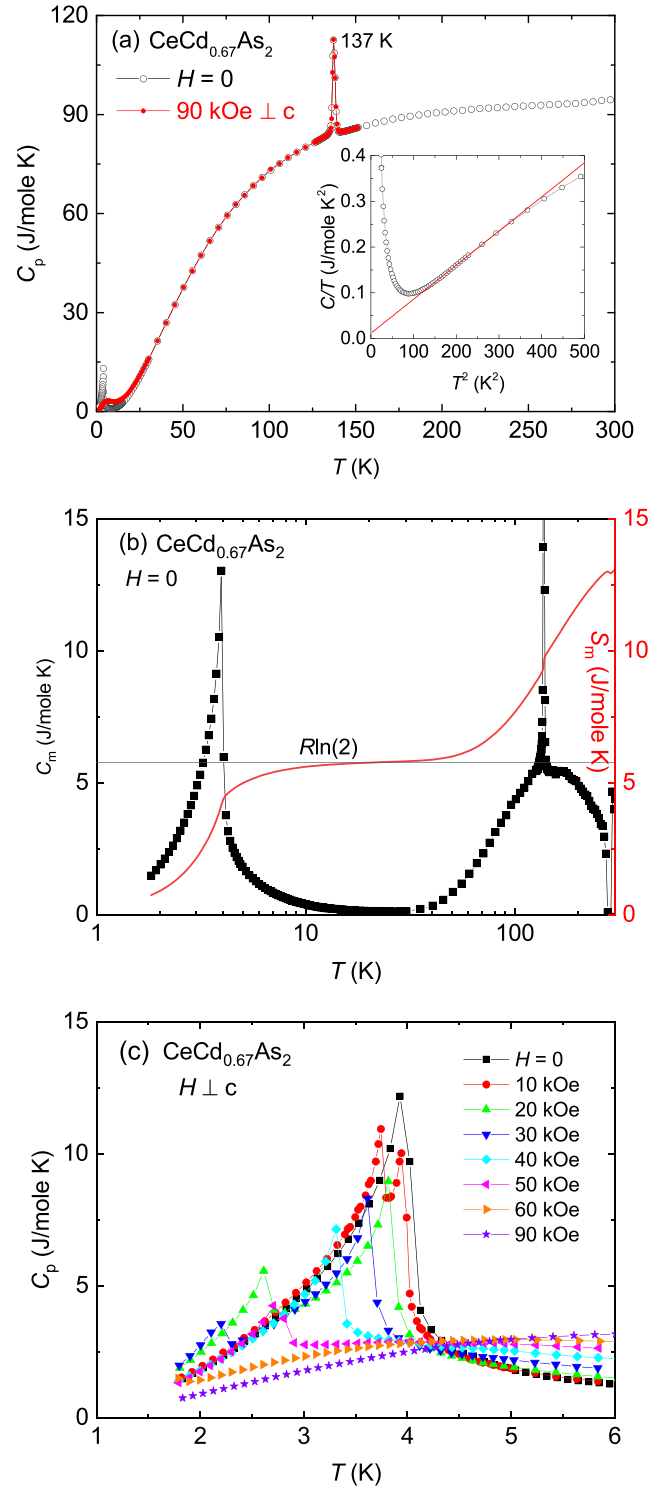
FIG. 6. (a) C_p of CeCd$_{0.67}$As$_2$ at $H = 0$ (open symbol) and 90 kOe (solid symbol) for $H \perp c$. Inset shows C/T vs T^2 plot. (b) C_m (symbol) and S_m (line) of CeCd$_{0.67}$As$_2$. (c) $C_p(T)$ below 6 K at selected magnetic fields.

and $\Theta_D = 212.7$ are estimated by fitting the curve above 10 K, as shown in the inset. The magnetic part of the specific heat C_m is plotted in Fig. 6(b), where C_p of LaCd$_{0.67}$As$_2$ is used

to estimate the nonmagnetic contribution to the specific heat of CeCd$_{0.67}$As$_2$. C_m shows a broad maximum centered around ~150 K, associated with the CEF splitting of the Hund's rule ground-state multiplet.

The magnetic entropy S_m is inferred by integrating C_m/T and plotted in Fig. 6(b). S_m reaches about 80% of $R\ln(2)$ at T_N and recovers the full doublet entropy by 20 K. This suggests that the sharp anomaly at 4 K in specific heat stems from the AFM order in a doublet ground state. In addition, the observed entropy implies that the ordered moment is not compensated by the Kondo interaction. At 300 K the recovered entropy is less than $R\ln(6)$, which suggests a large energy-level splitting due to the strong CEF effect.

In order to examine the effect of an applied magnetic field on the AFM order, the specific heat was measured for $H \perp c$ up to 90 kOe, plotted in Fig. 6(c). As the magnetic field increases, T_N shifts to lower temperatures and a second peak develops below T_N. For $H = 60$ kOe the phase transition is suppressed and instead C_p exhibits a broad maximum centered at 5 K, which marks a crossover from the AFM to paramagnetic state. At higher fields this maximum broadens further and moves to higher temperatures.

The $\rho(T)$ curves of CeCd$_{0.67}$As$_2$ are presented in Fig. 7(a), where two pieces of single crystals (sample 1 and 2) from the same batch are selected to examine the electrical resistivity. As the temperature decreases, $\rho(T)$ curves of both samples 1 and 2 increase slightly and indicate a sudden jump below $T_s = 136$ K, determined by the peak position in $d\rho(T)/dT$. At T_s, both samples indicate a hysteresis while warming and cooling the temperature, implying a first-order phase transition. For clarity, the hysteresis is shown only for sample 2 in the figure. Below T_s, the $\rho(T)$ curves show a sample dependence. $\rho(T)$ of sample 1 increases continuously with a hump at around 60 K and indicates a sharp drop below 4 K as a signature of AFM ordering, which is consistent with M/H and C_p measurements. The AFM phase transition temperature is determined to be $T_N = 4$ K from the peak position in $d\rho/dT$ analysis. The absolute value and temperature dependence of the resistivity for sample 1 are similar to that of CVT-grown Ce$_3$Cd$_2$As$_6$ [31,34], where the origin of the sudden jump at 137 K in $\rho(T)$ is suggested to be associated with the CDW transition. In contrast to sample 1, $\rho(T)$ of sample 2 shows a maximum near 120 K and decreases continuously. Although samples 1 and 2 show a different temperature dependence below T_s, both samples clearly indicate the anomaly at 4 K. The inset of Fig. 7(a) shows $\rho(T)$ curves of sample 2 at various magnetic fields, where T_N can be suppressed below 1.8 K at ~60 kOe. It should be emphasized that the electrical resistivity does not show a behavior typical of the Kondo lattice compounds. Specifically, no minimum or logarithmic upturn in $\rho(T)$ is observed.

The enhancement of $\rho(T)$ below T_s suggests a low carrier concentration in this system. As a further probe of the carrier density, ρ_H has been measured as a function of magnetic field and temperature. The ρ_H curves are basically linear in field and negative above 50 K, as shown in the inset of Fig. 7(b). R_H at $H = 90$ kOe is plotted in Fig. 7(b), where R_H is effectively temperature independent above $T_s = 137$ K and indicates a sharp drop below T_s. Based on the one-band model
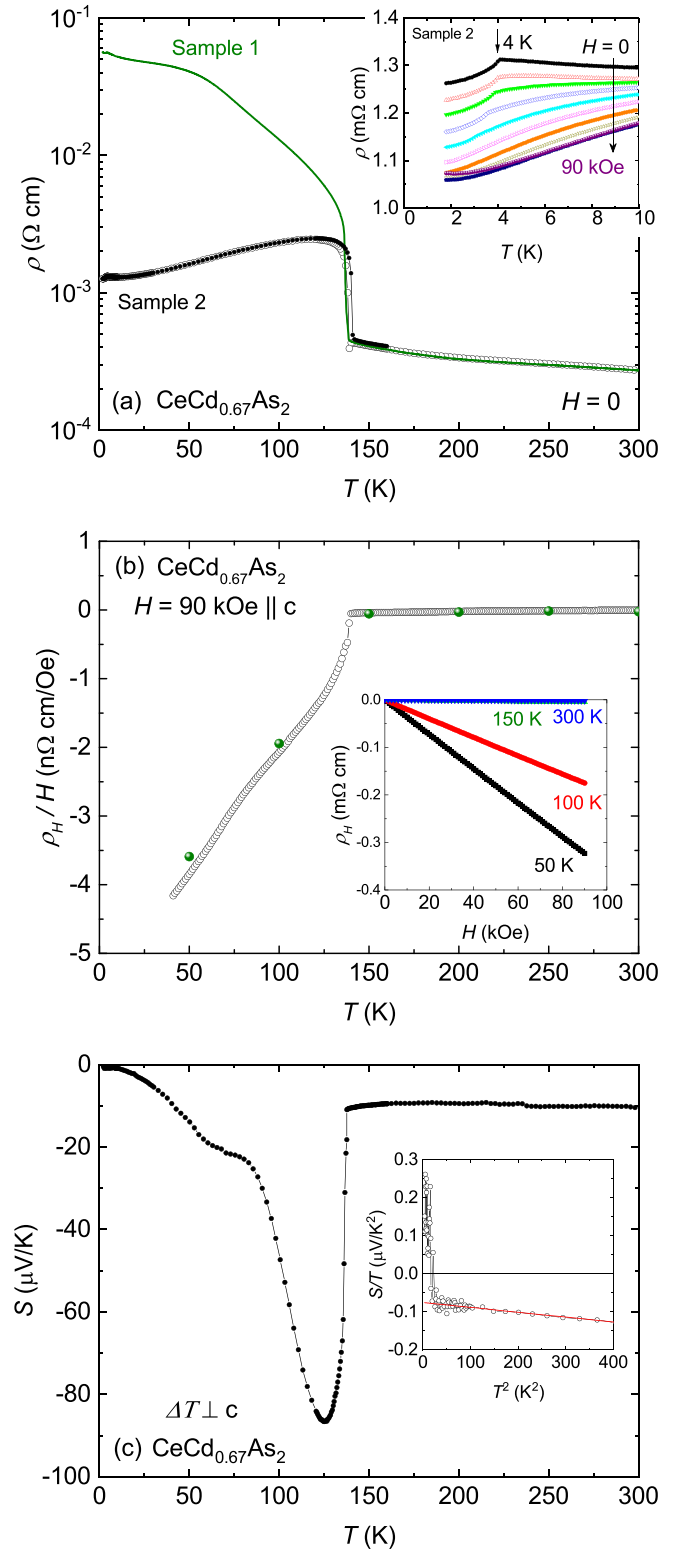

FIG. 7. (a) $\rho(T)$ of CeCd$_{0.67}$As$_2$ for samples 1 and 2. For the sample 2, open and closed symbols represent the resistivity data taken while cooling and warming the temperature. Inset shows $\rho(T)$ of sample 2 at various magnetic fields. (b) R_H at 90 kOe for $H \parallel c$. Solid symbols are taken from the magnetic field sweep data. Inset shows ρ_H at selected temperatures. (c) Zero field $S(T)$, taken while warming the sample. Inset shows S/T vs T^2 plot.

approximation, the carrier density is estimated to be $\sim 4.87 \times 10^{22}$ per cm^3 at 300 K and 1.62×10^{19} per cm^3 at 50 K. The negative sign of R_H indicates that transport is dominated by electronlike carriers. Figure 7(c) shows $S(T)$ of CeCd$_{0.67}$As$_2$, where sample 2 of the resistivity measurement was used for the TEP measurements. $S(T)$ depends weakly on temperature above T_s and shows a minimum near 120 K and a hump near 50 K. At low temperatures, $S(T)$ shows a sign change below ~ 4 K, coinciding with the AFM ordering temperature. Above T_N, $S(T)$ can be described by a $aT + bT^3$ relation, as shown in the inset. Since CeCd$_{0.67}$As$_2$ has magnetic Ce^{3+} ions, in addition to the diffusion and phonon drag, a contribution from the CEF to the TEP should be considered. In general, many Ce- and Yb-based Kondo lattice compounds show the extrema in $S(T)$ with enhanced value due to the Kondo effect in conjunction with the CEF effect. However, because $S(T)$ of CeCd$_{0.67}$As$_2$ shares a common temperature dependence with that of LaCd$_{0.67}$As$_2$ and the electrical resistivity shows no clear signature of Kondo contributions, we suggest that the broad minimum around 125 K is not associated with the Kondo effect.

For CeCd$_{0.67}$As$_2$, the strong magnetic anisotropy, broad maximum in the susceptibility for $H \parallel c$, reduced magnetization value at 70 kOe, and broad maximum in the specific heat suggest a large energy-level splitting of the $J = 5/2$ Hund's rule ground state of Ce ions. In the paramagnetic state the magnetic susceptibility curves are analyzed on the basis of the CEF (point charge) model [44]. Note that we assume the Hamiltonian below T_s remains the same, since the magnetic susceptibility changes a little below T_s and the in-plane magnetic anisotropy is small. The CEF Hamiltonian for the tetragonal symmetry can be expressed as $\mathcal{H}_{CEF} = B_2^0 O_2^0 + B_4^0 O_4^0 + B_4^4 O_4^4$, where B_n^m and O_n^m are the CEF parameters and Stevens operators [45,46], respectively. In the presence of an applied magnetic field, the Zeeman interaction must be included: $\mathcal{H}_{\text{Zeeman}} = -g_J \mu_B J_i H_i$, where g_J is the Landé g-factor, μ_B is the Bohr magneton, H_i is the applied magnetic field, and J_i is the angular momentum operator in the $i = x, y, z$ components. $M(H)$ for $H \parallel c$ and C_m at 90 kOe cannot be reproduced by using these two terms in the Hamiltonian. Therefore the molecular field terms are added into the total Hamiltonian: $\mathcal{H} = \mathcal{H}_{CEF} - g_J \mu_B J_i(H_i + \lambda_i M_i)$, where λ_i is the molecular field parameter and M_i is the magnetization. The eigenvalues E_n and the eigenfunctions $|n>$ are determined by diagonalizing the total Hamiltonian. The CEF parameters are initially obtained by fitting the magnetic susceptibility curves and determined by reproducing the measured specific heat and magnetization isotherms. From the analysis, it is found that the CEF ground state in CeCd$_{0.67}$As$_2$ is $|\pm 1/2>$, and the first and second excited levels are dominated by a combination of $|\pm 3/2>$ and $|\pm 5/2>$ states, as depicted schematically in Fig. 8(a).

The solid and dashed lines in Figs. 8(b)–8(d) are the calculated magnetic susceptibility, magnetization, and specific heat with the following fitted parameters: $B_2^0 = 19.35$ K, $B_4^0 = -1.05$ K, $B_4^4 = -5.46$ K, $\lambda_{\perp c} = 0.98$ mol/emu, and $\lambda_{\parallel c} = -22.82$ mol/emu. The observed anisotropy in $M(H)$ at 1.8 K is captured by the CEF model as shown in Fig. 8(b). Obviously, the calculation does not capture the MM transitions. The magnetic specific heat above 30 K is well explained by the
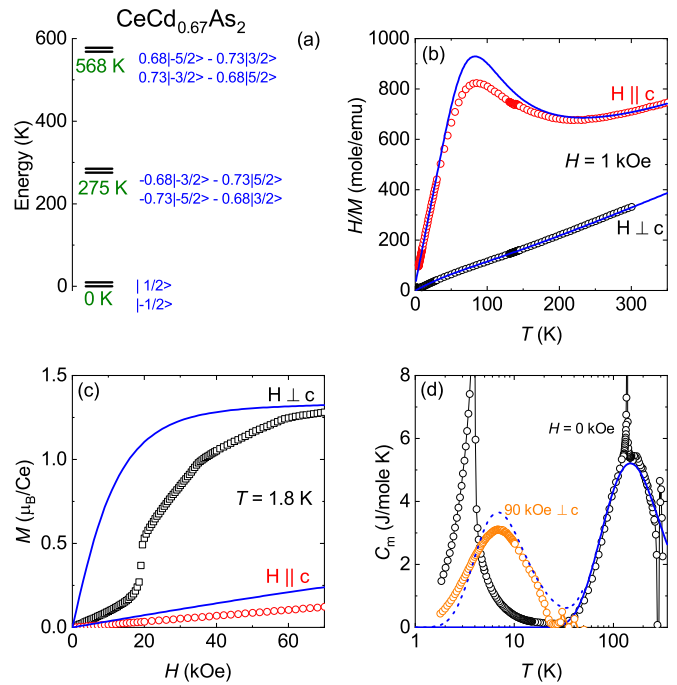

FIG. 8. (a) Schematic view of CEF energy levels and states. (b) Magnetic susceptibility at 1 kOe. (c) Magnetization at 1.8 K. (d) Specific heat at $H = 0$ and 90 kOe for $H \perp c$. Open symbols represent experimental data, and lines are from the CEF model (see text for details).

CEF model as shown in Fig. 8(d). The energy-level splitting $\Delta_1 = 275$ K and $\Delta_2 = 568$ K from the ground-state doublet to the first and second excited doublet is consistent with the entropy change shown in Fig. 6. In particular, for $H = 90$ kOe, the low-temperature broad maximum is reproduced, giving rise to a split of ground-state doublet via the Zeeman effect, implying well-localized $4f$ moments in CeCd$_{0.67}$As$_2$. It is clear from the analysis that in the paramagnetic state the magnetic property of CeCd$_{0.67}$As$_2$ can be well understood in the framework of CEF. In addition, the CEF analysis provides an evidence that the low-temperature magnetism of CeCd$_{0.67}$As$_2$ can be described by effective spin $J = 1/2$. It should be noted that due to the strong CEF contribution in the magnetic susceptibility curves, the obtained θ_p values from the high-temperature Curie-Weiss fit cannot be used to estimate the size of the magnetic interaction. The unusually large molecular field term $\lambda_{\parallel c}$ implies strong intralayer ferromagnetic exchange couplings. In the previous study, the CEF analysis of CVT-grown Ce$_3$Cd$_2$As$_6$ was performed by including spin-exchange interaction terms [with AFM contribution for $H \perp c$ and ferromagnetic (FM) for $H \parallel c$], but only reproducing the MM transition at 34 kOe [34]. It seems that the large intralayer FM coupling plays a crucial role in the MM transitions.

Figure 9 shows the phase transition temperatures and fields determined from magnetization, resistivity, and specific heat measurements, where symbols are extracted from $d\chi T/dT$, $d\rho/dT$, dM/dH, and $C_p(T, H)$. As shown in the phase diagram, the critical temperature determined from temperature sweeps tracks well the critical field determined from field sweeps. The phase transition can be traced by a line which is
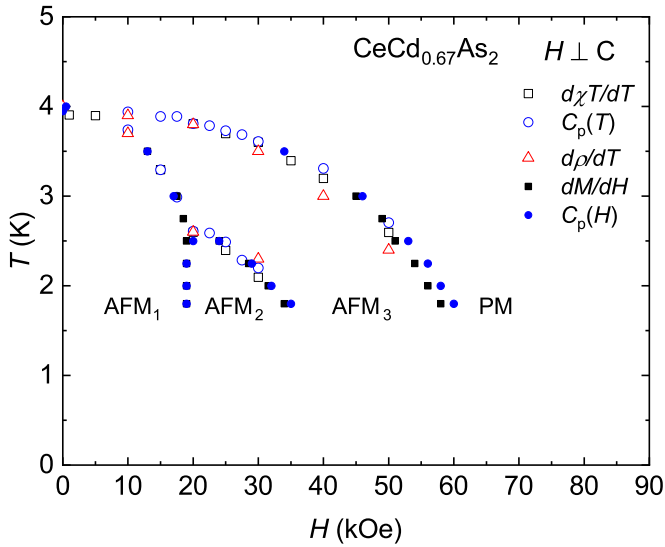
FIG. 9. $H - T$ phase diagram of CeCd$_{0.67}$As$_2$ for $H \perp c$.

connected from $T_N = 4$ K at $H = 0$ to the critical field $H_c \sim$ 60 kOe at $T = 1.8$ K for $H \perp c$. Additional phase boundaries emerge inside the AFM boundary as the magnetic field increases. In spite of the abrupt changes in magnetization isotherms, no hysteresis is detected at the phase boundaries. Although further measurements below 1.8 K are required, no non-Fermi-liquid behavior is observed near the critical field due to a negligible Kondo effect. The extremely low carrier density, probably due to the distortion of the As-square net, leaving only a few carriers in the conduction band, prevents the formation of a Kondo singlet. When the concentration of charge carriers is controlled by doping, it would be interesting to investigate whether the Kondo effect turns on. Optical tuning of wide-range carrier density is an alternative way to observe the photoinduced Kondo effect as observed in the CeZn$_3$P$_3$ semiconductor [47]. Nevertheless, RKKY interaction may be responsible for the AFM ordering; however, it would have to be mediated by extremely low charge carriers. When pressure is applied, the electrical resistivity recovers a metallic behavior and the magnetic ordering temperature increases [31]. The enhancement of T_N under pressure can be naturally explained as arising from increased carrier concentrations.

The resistivity of LaCd$_{0.67}$As$_2$ shows an anomaly at around $T_s = 280$ K, which most likely has the same origin as the $T_s = 137$ K anomaly seen in CeCd$_{0.67}$As$_2$. By assuming that the high-temperature transition is caused by the formation of CDW, suggested in Ref. [34], an interesting question arises as to how the CDW and long-range magnetic order interact or compete. It is necessary to perform scattering experiments to identify the origin of T_s as well as the interaction between CDW and long-range magnetic order. When electrical resistivity and Hall resistivity are compared, a relatively high mobility of charge carriers ($\sim$240 cm^2/Vs at 50 K) suggests an unusual electronic state below T_s.

IV. SUMMARY

We have studied thermodynamic and transport properties of the single crystals of RCd$_{0.67}$As$_2$ ($R =$ La and Ce). LaCd$_{0.67}$As$_2$ shows a (structural) phase transition at $T_s \sim$ 280 K below which transport properties are governed by an extremely low carrier density. CeCd$_{0.67}$As$_2$ exhibits a phase transition at 137 K accompanied by semiconductorlike enhancement of the electrical resistivity and indicates an AFM phase transition at 4 K. CeCd$_{0.67}$As$_2$ manifests a large magnetic anisotropy. The specific heat data, together with the anisotropic magnetization, was analyzed on the basis of the point charge model of the crystalline electric field. In the paramagnetic phase, the observed magnetic behaviors are well explained by the CEF effects. Although the AFM phase transition temperature in CeCd$_{0.67}$As$_2$ can be continuously suppressed by the magnetic field to zero, the highly localized $4f$ moments with extremely low charge carriers prevent observation of the quantum critical fluctuations shown in many Ce-based materials.

[1] G. R. Stewart, Rev. Mod. Phys. **56**, 755 (1984).

[2] J. M. Lawrence, P. S. Riseborough, and R. D. Parks, Rep. Prog. Phys. **44**, 1 (1981).

[3] F. Steglich, J. Aarts, C. D. Bredl, W. Lieke, D. Meschede, W. Franz, and H. Schäfer, Phys. Rev. Lett. **43**, 1892 (1979).

[4] Y. Ōnuki, R. Settai, K. Sugiyama, T. Takeuchi, T. C. Kobayashi, Y. Haga, and E. Yamamoto, J. Phys. Soc. Jpn. **73**, 769 (2004).

[5] R. Settai, T. Takeuchi, and Y. Ōnuki, J. Phys. Soc. Jpn. **76**, 051003 (2007).

[6] C. Pfleiderer, Rev. Mod. Phys. **81**, 1551 (2009).

[7] P. Gegenwart, Q. Si, and F. Steglich, Nat. Phys. **4**, 186 (2008).

[8] P. Coleman, Phys. Status Solidi B **247**, 506 (2010).

[9] Z. F. Weng, M. Smidman, L. Jiao, X. Lu, and H. Q. Yuan, Rep. Prog. Phys. **79**, 094503 (2016).

[10] P. Nozières, Eur. Phys. J. B **6**, 447 (1998).

[11] Th. Pruschke, R. Bulla, and M. Jarrell, Phys. Rev. B **61**, 12799 (2000).

[12] T. Takabatake, G. Nakamoto, T. Yoshino, H. Fujii, K. Izawa, S. Nishigori, H. Goshima, T. Suzuki, T. Fujita, K. Maezawa, T. Hiraoka, Y. Okayama, I. Oguro, A. A. Menovsky, K. Neumaier, A. Brückl, and K. Andres, J. Phys. B: Condens. Matter **223-224**, 413 (1996).

[13] S. Nishigori, H. Goshima, T. Suzuki, T. Fujita, G. Nakamoto, H. Tanaka, T. Takabatake, and H. Fujii, J. Phys. Soc. Jpn. **65**, 2614 (1996).

[14] M. F. Hundley, P. C. Canfield, J. D. Thompson, Z. Fisk, and J. M. Lawrence, Phys. Rev. B **42**, 6842 (1990).

[15] Y. Luo, F. Ronning, N. Wakehama, X. Lu, T. Park, Z.-A. Xu, and J. D. Thompson, Proc. Natl. Acad. Sci. USA **112**, 13520 (2015).

[16] J. Chen, Z. Wang, Y. Li, C. Feng, J. Dai, Z. Xu, and Q. Si, Sci. Rep. **9**, 12307 (2019).

[17] B. K. Rai, I. W. H. Oswald, W. Ban, C.-L. Huang, V. Loganathan, A. M. Hallas, M. N. Wilson, G. M. Luke, L. Harriger, Q. Huang, Y. Li, S. Dzsaber, J. Y. Chan, N. L. Wang, S. Paschen, J. W. Lynn, A. H. Nevidomskyy, P. Dai, Q. Si, and E. Morosan, Phys. Rev. B **99**, 085120 (2019).

[18] P. S. Riseborough, Adv. Phys. **49**, 257 (2000).

[19] Y. Tokiwa, C. Stingl, M.-S. Kim, T. Takabatake, and P. Gegenwart, Sci. Adv. **1**, e1500001 (2015).

[20] S. Dzsaber, L. Prochaska, A. Sidorenko, G. Eguchi, R. Svagera, M. Waas, A. Prokofiev, Q. Si, and S. Paschen, Phys. Rev. Lett. **118**, 246601 (2017).

[21] M. Brylak, M. H. Möller, and W. Jeitschko, J. Solid State Chem. **115**, 305 (1995).

[22] A. Leithe-Jasper and P. Rogl, J. Alloys Compd. **203**, 133 (1994).

[23] O. Sologub, K. Hiebl, P. Rogl, and O. Bodak, J. Alloys Compd. **227**, 40 (1995).

[24] K. D. Myers, S. L. Bud'ko, I. R. Fisher, Z. Islam, H. Kleinke, A. H. Lacerda, and P. C. Canfield, J. Magn. Magn. Mater. **205**, 27 (1999).

[25] S. S. Stoyko and A. Mar, J. Solid State Chem. **184**, 2360 (2011).

[26] C. Petrovic, S. L. Bud'ko, J. D. Strand, and P. C. Canfield, J. Magn. Magn. Mater. **261**, 210 (2003).

[27] G. Cordier, H. Schäfer, and P. Woll, Z. Naturforsch. B **40**, 1097 (1985).

[28] A. T. Nientiedt and W. Jeitschko, J. Solid State Chem. **142**, 266 (1999).

[29] M. Eschen and W. Jeitschko, Z. Naturforsch. B **58**, 399 (2003).

[30] M. Wang, R. McDonald, and A. Mar, J. Solid State Chem. **147**, 140 (1999).

[31] M. M. Piva, M. C. Rahn, S. M. Thomas, B. L. Scott, P. G. Pagliuso, J. D. Thompson, L. M. Schoop, F. Ronning, and P. F. S. Rosa, Chem. Mater. **33**, 4122 (2021).

[32] E. V. Sampathkumaran, K. Sengupta, S. Rayaprol, K. K. Iyer, Th. Doert, and J. P. F. Jemetio, Phys. Rev. Lett. **91**, 036603 (2003).

[33] D. Evans, S. Dunsiger, and E. Mun, Phys. Rev. B **105**, 085105 (2022).

[34] M. M. Piva, L. Xiang, J. D. Thompson, S. L. Bud'ko, R. A. Ribeiro, P. C. Canfield, and P. F. S. Rosa, Phys. Rev. B **105**, 094443 (2022).

[35] S. R. Dunsiger, J. Lee, J. E. Sonier, and E. D. Mun, Phys. Rev. B **102**, 064405 (2020).

[36] W. Tremel and R. Hoffmann, J. Am. Chem. Soc. **109**, 124 (1987).

[37] Z. H. Dughaish, Phys. B: Condens. Matter **322**, 205 (2002).

[38] Z. M. Gibbs, H.-S. Kim, H. Wang, and G. Jeffrey Snyder, Appl. Phys. Lett. **106**, 022112 (2015).

[39] I. T. Witting, T. C. Chasapis, F. Ricci, M. Peters, N. A. Heinz, G. Hautier, and G. Jeffrey Snyder, Adv. Electron. Mater. **5**, 1800904 (2019).

[40] K. Behnia, D. Jaccard, and J. Flouquet, J. Phys.: Condens. Matter **16**, 5187 (2004).

[41] F. J. Blatt, P. A. Schroeder, C. L. Foiles, and D. Greig, *Thermoelectric Power of Metals* (Plenum, New York, 1976).

[42] D. Rutzinger, C. Bartsch, M. Doerr, H. Rosner, V. Neu, Th. Doert, and M. Ruck, J. Solid State Chem. **183**, 510 (2010).

[43] C. Song, J. Park, J. Koo, K.-B. Lee, J. Y. Rhee, S. L. Bud'ko, P. C. Canfield, B. N. Harmon, and A. I. Goldman, Phys. Rev. B **68**, 035113 (2003).

[44] A. Scheie, J. Appl. Crystallogr. **54**, 356 (2021).

[45] M. T. Hutchings, Solid State Phys. **16**, 227 (1964).

[46] K. W. H. Stevens, Proc. Phys. Soc. A **65**, 209 (1952).

[47] J. Kitagawa, D. Kitajima, K. Shimokawa, and H. Takaki, Phys. Rev. B **93**, 035122 (2016).